Wheel-rail rolling contact behavior induced by both rail surface irregularity and sleeper hanging defects on a high-speed railway line

Yang, Fei; Wei, Zilong; Sun, Xianfu; Shen, Chen; Núñez, Alfredo

DOI
10.1016/j.engfailanal.2021.105604

Publication date
2021

Document Version
Final published version

Published in
Engineering Failure Analysis

Engineering Failure Analysis 128 (2021) 105604

Contents lists available at ScienceDirect

Engineering Failure Analysis

journal homepage: www.elsevier.com/locate/engfailanal

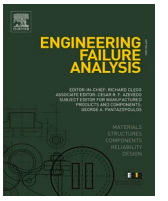

Wheel-rail rolling contact behavior induced by both rail surface irregularity and sleeper hanging defects on a high-speed railway line

Fei Yang [a], Zilong Wei [a], Xianfu Sun [a], Chen Shen [b], Alfredo Núñez [b,*]

[a] Infrastructure Inspection Research Institute, China Academy of Railway Sciences Corporation Limited, China
[b] Section of Railway Engineering, Department of Engineering Structures, Faculty of Civil Engineering and Geosciences, Delft University of Technology, the Netherlands

ARTICLE INFO

Keywords:
Sleeper hanging
Uneven settlement
Wheel-rail rolling contact
Rail degradation

ABSTRACT

In this study, a wheel-rail transient rolling contact model capable of accounting for the nonlinear displacement-force properties of hanging sleepers is proposed. The sleeper hanging status affected by rail irregularities is an input for an analysis of the wheel-rail contact behavior and related rail degradation in terms of plastic deformation and rolling contact fatigue. The results indicate that the severity of sleeper hanging is significantly affected by the geometric characteristics and the relative position with respect to the sleepers of the rail surface irregularity. The sleeper hanging defects aggravate the wheel-rail impact and increase the wheel-rail contact force amplitude, contact patch size, pressure, and von Mises stress, thus exacerbating the plastic deformation of the rail material. It was also found that the sleeper hanging defects rarely affect the distribution of the adhesion-slip states and rolling contact fatigue. The knowledge gained can serve as guidance for evaluating the condition and conducting the maintenance of ballasted railway tracks.

1. Introduction

The quality of track geometry is essential for the dynamic behavior of rolling stocks. The presence of initial deformation on the rail surface (see the examples shown in Fig. 1) inherently causes abnormal vibrations and exacerbates the deterioration of track components. For newly built ballasted railways, high wheel-rail impact loads at rail surface irregularities have a higher likelihood of causing rail substructure defects, such as the uneven settlement of trackbeds and hanging sleepers, since the granular trackbed is relatively loose at the initial stage of the whole service life. Consequently, the smoothness of the track geometry would further deteriorate during the passage of vehicles, speeding up rail degradation and even endangering train operation safety.

In the literature, extensive efforts have been made to investigate sleeper hanging defects and their influence on dynamic vehicle-track interactions. Grassie [1] examined the dynamic response of a railway track with a section of unsupported sleepers and found that the deflections of the fastening system and sleeper strains increase significantly due to the absence of ballast. Kaewunruen et al. [2,3] studied the uneven settlement of the trackbed on the sleeper hanging behavior and the related vibration characteristics by combining finite element (FE) simulation with field experiments. Similar approaches were proposed in [4-8], where the effects of sleeper hanging

* Corresponding author.
E-mail addresses: 13811807268@163.com (F. Yang), weizilong@rails.cn (Z. Wei), sunxianfu@rails.cn (X. Sun), C.Shen-2@tudelft.nl (C. Shen), A.A.NunezVicencio@tudelft.nl (A. Núñez).

https://doi.org/10.1016/j.engfailanal.2021.105604
Received 13 April 2021; Received in revised form 6 July 2021; Accepted 10 July 2021
Available online 14 July 2021

on the dynamic behavior of railway tracks were investigated. Regarding the contribution of sleeper hanging on the dynamic vehicle-track response, Sadri et al. [9,10] developed a frequency-domain model capable of analyzing the nonuniformity of track properties to quantify the effect of sleeper hanging on the mechanical energy dissipated of a track system under moving loads. Zhu et al. [11] proposed a numerical approach to investigate the dynamic response of wheel/rail components due to single or multiple unsupported sleepers and found that the vehicle speed, gap size, and number of hanging sleepers are essential to dictate the magnitude of the impact loads. Dahlberg [12] analyzed the long-term settlement behavior of the trackbed using an explicit FE method and numerically reproduced the development of sleeper hanging. Varandas et al. [13] developed an incremental settlement model to investigate the loss of contact between the sleepers and ballast and the long-term settlement behavior of the ballast.

The above studies mainly focused on the cause of sleeper hanging and its consequences, whereas only a few account for the integrated effects of sleeper hanging defects and rail surface irregularities on the wheel-rail contact behavior. In the literature, the dynamic wheel-rail interaction is commonly estimated by either multibody dynamics (MBD) or FE methods. Generally, the MBD method adopts the (semi/multi) Hertz theory for the normal contact solution, while Kalker's method FASTSIM is used for the tangent solution [14-16] with the assumptions of half-space, linear elasticity, and steady-state. Restricting to these assumptions, the MBD method is challenged when dealing with the plastic deformation and impact interaction of the contact bodies. Alternatively, these assumptions can be relaxed with the use of FE methods. Li et al. [17–19] proposed a 3D wheel-rail transient rolling contact model using an explicit FE method and simulated wheel-rail impact behavior at squats on straight tracks. Similar approaches have also been successfully employed to investigate the dynamic wheel-rail interaction for more generalized defect types, such as insulated rail joints [20], poor rail welds [21], and degraded crossing rails [22]. At present, applications of the wheel-rail transient rolling contact model mainly focus on the short-wavelength irregularities occurring at the wheel/rail interface, whereas few of them account for the deterioration of the rail substructure components.

In this study, a wheel-rail rolling contact model capable of accounting for the nonlinear displacement-force properties of sleeper hanging defects is developed using the FE method. The effect of rail surface irregularities on the dynamic interactions of wheel/rail and sleeper/ballast is investigated, and the uneven settlement of the trackbed is extracted. After that, the wheel-rail rolling contact behavior affected by the combination of rail surface irregularity and sleeper hanging defects is simulated, and the simulated contact parameters serve as an input for the analysis of rail degradation in terms of plastic deformation and rolling contact fatigue (RCF). The proposed method provides further understanding of hanging sleeper defects and is useful for the design of maintenance decision-making strategies. The structure of this paper is as follows. Section 2 illustrates the methodology. Section 3 analyzes the sleeper hanging defects induced by rail surface irregularity. Section 4 investigates the wheel-rail rolling contact behavior and related rail degradation induced by both sleeper hanging defects and the rail surface irregularity. Finally, Section 5 addresses the main conclusions and further research.

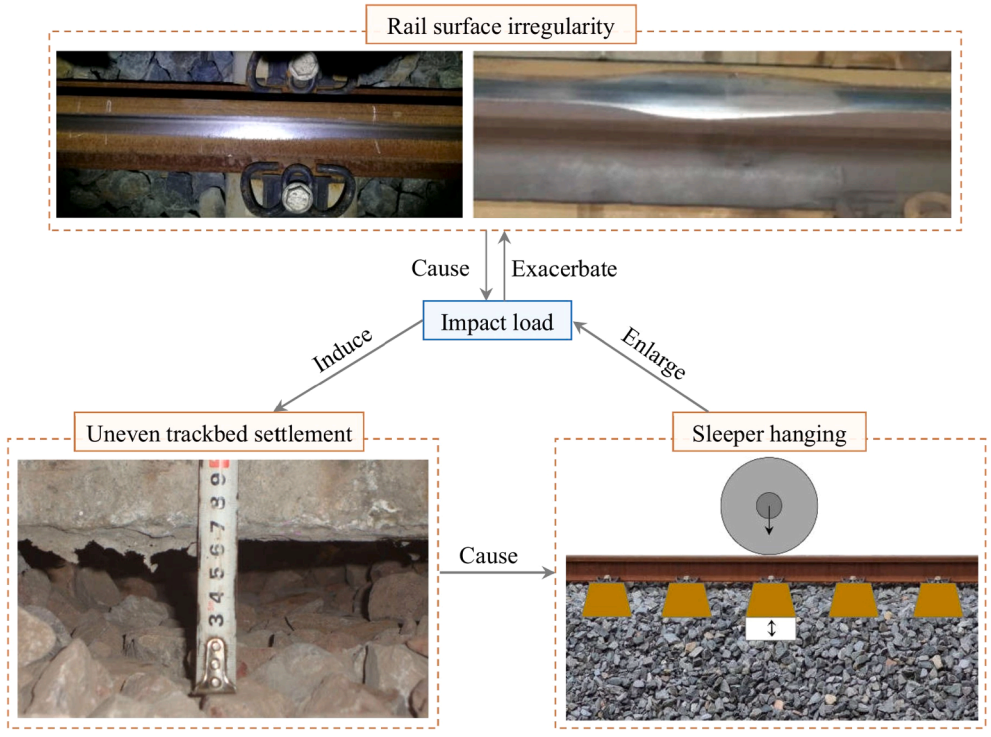

Fig. 1. Interaction between a rail surface irregularity and a hanging sleeper. The variations in the width of the shiny running band indicate rail surface irregularity.

2. Methodology

This section introduces a method to analyze sleeper hanging defects induced by a rail surface irregularity and the consequences for wheel-rail rolling contact behavior. The method is composed of 1) an FE simulation of the dynamic wheel-track interaction at rail surface irregularities, 2) an evaluation of the uneven settlement of the trackbed and the resulting sleeper hanging defects during long-term usage, and 3) an FE simulation of the wheel-rail contact behavior and the related rail degradation.

2.1. In situ measurement of rail surface irregularities

In situ measurements were conducted on ballasted HSR track sites with rapid geometry deterioration (e.g., the case shown in Fig. 1). Fig. 2 shows the details of the rail surface irregularities at eight different 1-m long track sections. In the figure, the amplitudes of the irregularities are in the range of 0.36 ~ 0.53 mm, and the waveform can be classified into two types: unimodal and bimodal irregularities.

In this paper, the rail surface irregularities are input for the FE simulation. For an easier comparison among different scenarios, the rail surface irregularities are generalized, as shown in Fig. 3. The unimodal type is modeled by a cosine function $Y_V(x)$, while a piecewise function $Y_W(x)$ models the bimodal type; see Equations (1) and (2). In the FE modeling, a set of combinations of wave depth and wavelength is considered.

$$Y_V(x) = \frac{a_1}{2}\left(cos\frac{2\pi x}{L} - 1\right), \quad 0 \leqslant x \leqslant L \tag{1}$$

$$Y_W(x) = \begin{cases} \dfrac{a_1}{2}\left(cos\pi\dfrac{x}{\lambda} - 1\right), & 0 \leqslant x < \lambda \\ \dfrac{a_2 - a_1}{2} cos\left(2\pi\dfrac{x-\lambda}{L-2\lambda}\right) - \dfrac{a_1 + a_2}{2}, & \lambda \leqslant x < (L-\lambda) \\ -\dfrac{a_1}{2}\left(cos\pi\dfrac{x - L + \lambda}{\lambda} + 1\right), & (L-\lambda) \leqslant x \leqslant L \end{cases} \tag{2}$$

where L represents the wavelength of the rail surface irregularity, a_1 indicates the amplitude of the rail surface irregularity, and a_2 and λ are parameters used to define the geometry of the bimodal irregularity.

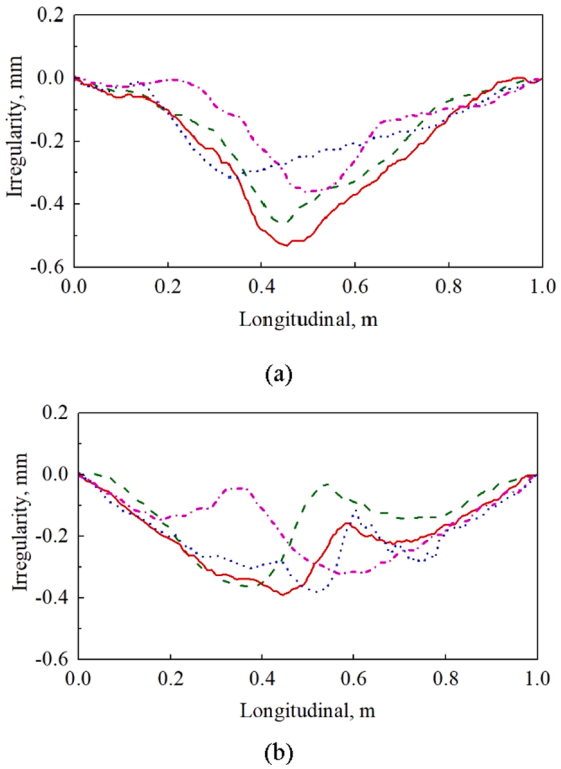

Fig. 2. Measured rail surface irregularities. (a) Unimodal type, (b) Bimodal type.

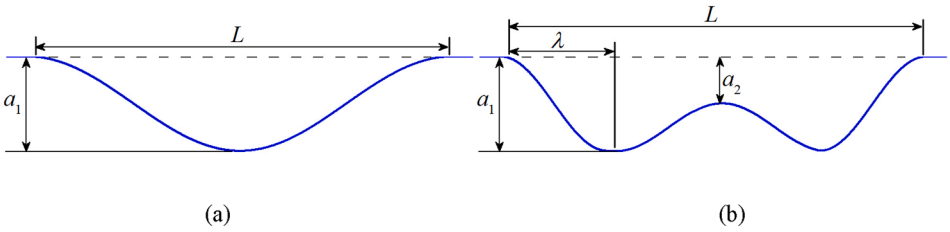

Fig. 3. Modeled geometry of rail surface irregularity: (a) unimodal type, (b) bimodal type.

2.2. FE simulation of the dynamic wheel-track interaction

The passage of one wheel over a plain ballasted track is simulated using the commercial software ANSYS/LS-DYNA, as shown in Fig. 4. The presence of rail surface irregularities excites high-frequency vibrations of wheels and rails, especially under high train speeds [23]; therefore, the flexibility of the contact bodies is included by modeling the wheel as a continuum while simplifying the bogie frame and car body as a lumped mass. The wheel profile is LMA, and the wheel diameter is 860 mm. The wheel mass M_w is 586 kg, and the lumped mass M_c is 7414 kg. The primary suspension is modeled as linear springs and viscous dampers with the types of COMBIN14 in ANSYS and COMBI165 in LS-DYNA, and the stiffness K_p and damping C_p of the primary suspension are 0.88 MN/m and 4 kN•s/m, respectively. For the track model, the rail and sleepers are modeled with solid elements, while both the railpads and ballast are simplified as linear springs and viscous dampers. The rail profile is CN60, the rail inclination is 1:40, and the sleeper span is 0.60 m.

Railpads and ballast are modeled using the same element types as the primary suspension. The stiffness K_f and damping C_f are 22 MN/m and 60 kN•s/m for a standard railpad, while the corresponding values K_b and C_b of the ballast are 150 MN/m and 600 kN•s/m, respectively, for a standard concrete sleeper. The length of the crossing model was 12.6 m, which is equal to 21 sleeper spans and has proven to be reasonable for the wheel-rail impact at short-wave rail irregularities [19]. The model considers half of the wheelset and the track structure, and the lateral movement of the wheel is neglected.

The mesh of the FE model is shown in Fig. 4(b), where the wheel, rail, and sleepers are modeled by hexahedral solid elements with the types SOLID185 in ANSYS and SOLID164 in LS-DYNA. The minimum element size is set to 1 × 1 mm at the wheel/rail interface. The wheel/rail material adopts a bilinear elastic constitutive model to consider the nonlinear deformation under impact loads. The density, Young's modulus, Poisson's ratio and tangent modulus of the wheel and rail are 7790 kg/m^3, 206 GPa, 0.3 and 20.6 GPa, respectively. A linear elastic material is specified for the sleepers, with the density, Young's modulus, and Poisson's ratio being 2400 kg/m^3, 36 GPa and 0.3, respectively. The wheel-rail normal contact adopts the penalty contact algorithm, while the friction in the tangent contact is determined by Coulomb's law of friction. The friction coefficient is set to 0.4 for clean and dry conditions. The translational/rotational velocities are specified on the vehicle model, and the driving torque T is specified on the axis of the wheelset using Hughes-Liu beam elements [24] (with the type BEAM161 in LS-DYNA). The value of the driving torque is determined by the

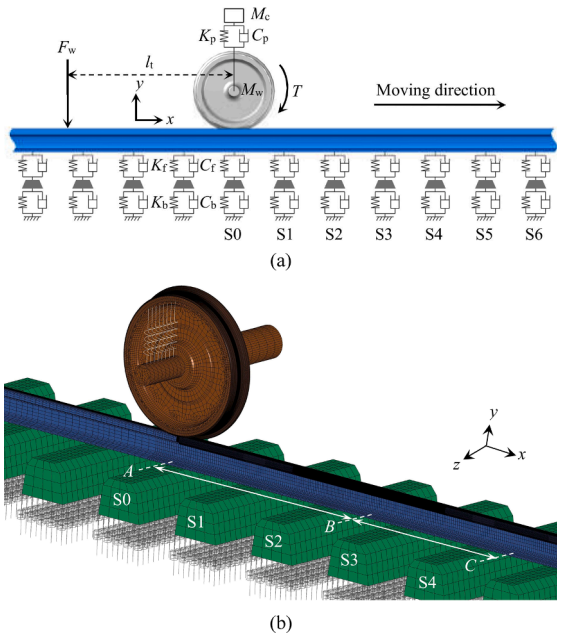

Fig. 4. 3D FE model for wheel-rail rolling contact, (a) overview, (b) mesh of the wheel, rail, and sleepers.

traction coefficient, i.e., the wheel/rail tangential contact force multiplied by the normal contact forces. In this study, the traction coefficient is 0.15. Note that the traction coefficient fluctuates slightly due to structural vibrations during the dynamic wheel-rail interaction. The rail model employs nonreflecting boundary conditions to eliminate the disturbance of wave reflection at the boundaries as much as possible.

In this study, only one passage of the wheels is simulated, which is mainly restricted by the time-consuming calculation process of the explicit FE method. In FE modeling, the geometry of the rail surface irregularity is introduced by modifying the y-coordinate of the nodes at the surface and subsurface of the rail head. An existing study [25] indicates that the explicit scheme remains stable if the volume fluctuations of the modified rail elements are below 15%. The explicit integration scheme employs the central difference method, and the integration time step is 0.9 times the critical time step, which is dominated by the smallest element size of the FE model. In the explicit simulation, the integration time step equals 2.3×10^{-8} s. Since the dynamic load of an adjacent wheel in the same bogie has a nonnegligible effect on the deflection of sleepers and ballast, an additional moving wheel load F_w is applied on the rail (see Fig. 4(a)). The distance between the additional moving load and the wheel axle l_t is 2.5 m, while the magnitude and loading position of F_w are obtained by the simulation of wheel-rail transient interaction, which is illustrated in Section 2.5. A typical explicit FE simulation takes approximately 9 h by using 18 cores of Intel Xeon Gold 6154 3.0 GHz CPU. During this period, the wheelset with a speed of 250 km/h rolls 3.6 m along the rail, in which 6 sleeper spans are included.

2.3. Modeling of the settlement of the trackbed

The sleeper and the ballast are in a close fit state under nominal conditions. With the accumulation of traffic loads, the trackbed undergoes settlement during long-term service. In regions with rail surface irregularities, uneven settlement may occur due to impact loads, consequently leading to sleeper hanging defects. In the literature, several empirical models are available to predict the settlement of trackbeds, e.g., Alva-Hurtado's model, ORE's model, Holzlohner's model, Shenton's model, Sato's model, and Hettler's model [12,13,26]. The logarithmic function proposed by Hettler [27] describes the displacement settlement, and its capability has been demonstrated for reproducing the development of sleeper hanging on Chinese high-speed railway lines [28]. Therefore, Hettler's model is employed in this study, in which the settlement of the trackbed after a large number of loading cycles is dependent on the settlement after the first cycle, expressed as:

$$u_N = sF_b^{1.6}[1 + c\ln(N)] \tag{3}$$

where u_N is the ballast settlement (mm), F_b is the amplitude of the sleeper-ballast force at the first loading cycle (kN), N is the number of loading cycles, s is a scaling factor equal to 9.5×10^{-4} mm/kN$^{1.6}$, and c is a model parameter with a value of 0.43 [12].

2.4. Modeling of nonlinear properties of hanging sleepers

A nonlinear spring is introduced to simulate the sleeper hanging behavior influenced by the uneven settlement of the trackbed, as shown in Fig. 5. Compared with the model proposed in [13,29], this study also considers the initial displacement of the hanging sleepers and their superstructure under gravity. As a consequence, the estimation of the sleeper hanging status is closer to realistic conditions, which contributes to the analysis of dynamic sleeper-ballast interactions at deteriorated track sites. The supporting force of the ballast under sleeper i, $F_{b,i}$, and the hanging distance of sleeper i, δ_i, are given by:

$$F_{b,i} = \begin{cases} K_b\left(Y_{b,i} - \delta_i\right), & Y_{b,i} > \delta_i \\ 0, & Y_{b,i} \leqslant \delta_i \end{cases} \tag{4}$$

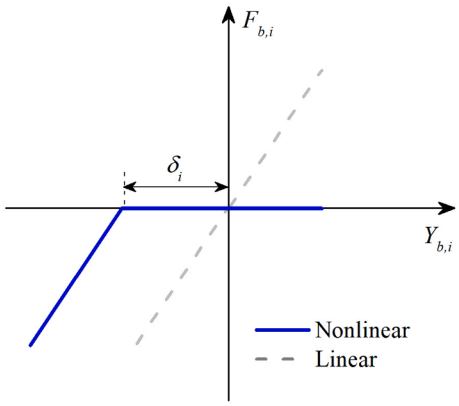

Fig. 5. Nonlinear force–displacement behavior of the springs under hanging sleepers.

$$\delta_i = \begin{cases} \Delta u_{N,i} - \Delta Y_{s,i},\ \Delta u_{N,i} > \Delta Y_{s,i} \\ 0,\ \Delta u_{N,i} \leqslant \Delta Y_{s,i} \end{cases} \tag{5}$$

where K_b is the vertical stiffness of the ballast, $Y_{b,i}$ is the displacement of sleeper i during the vehicle passing by, $\Delta u_{N,i}$ is the amplitude of uneven ballast settlement at sleeper i, and $\Delta Y_{s,i}$ is the relative displacement of sleeper i under gravity between nominal and hanging conditions. Note that Equation (4) focuses on the nonlinear relation between spring force and sleeper/ballast displacement, while the nonlinear property of the damping force is excluded.

2.5. Calculation procedure

The calculation procedure of the methodology is as follows:

Step 1: The static equilibrium of the vehicle standing still on the ballasted track is calculated using the implicit integration algorithm of ANSYS. After that, we introduce the static equilibrium as the initial condition and reproduce the dynamic vehicle-track interaction using the explicit integration algorithm of LS-DYNA. In the explicit FE simulation, the geometry of rail surface irregularity is considered an input, and the translational/rotational velocities and the driving torque are specified on the vehicle model. The normal solution of wheel-rail contact is used to assembly the moving load F_w, which is the phase delay with respect to the leading wheel and aims to take the influence of sleeper hanging into full consideration.

Step 2: The additional moving load F_w is introduced into the FE simulation, and the distributions of contact force between the leading wheel and the rail as well as between the sleeper and the ballast are calculated via the implicit-explicit simulation process.

Step 3: The trackbed settlement is extracted using Equation (3) under specified traffic loads and the hanging status of the sleepers affected by rail surface irregularities is evaluated.

Step 4: The nonlinear force–displacement properties of hanging sleeper defects are introduced into the FE modeling, and steps 1 and 2 are repeated to simulate the wheel-rail transient contact behavior and rail degradation.

In total, the implicit-explicit simulations were conducted 4 times in the calculation procedure.

3. Sleeper hanging defects induced by rail surface irregularity

This section analyzes the dynamic wheel-track interaction at rail surface irregularities and investigates the sleeper hanging status under specified traffic loads. The analysis considers the unimodal and bimodal types of rail surface irregularities, which occur at two typical positions: 1) above sleeper S3 and 2) in the middle of sleepers S3 and S4 (see Fig. 4(a)). Regarding the geometry of rail surface irregularity, the wavelength L is set to 1.0 m, and the wave depth a_1 varies from 0.1 mm to 0.5 mm. The parameter λ for the bimodal

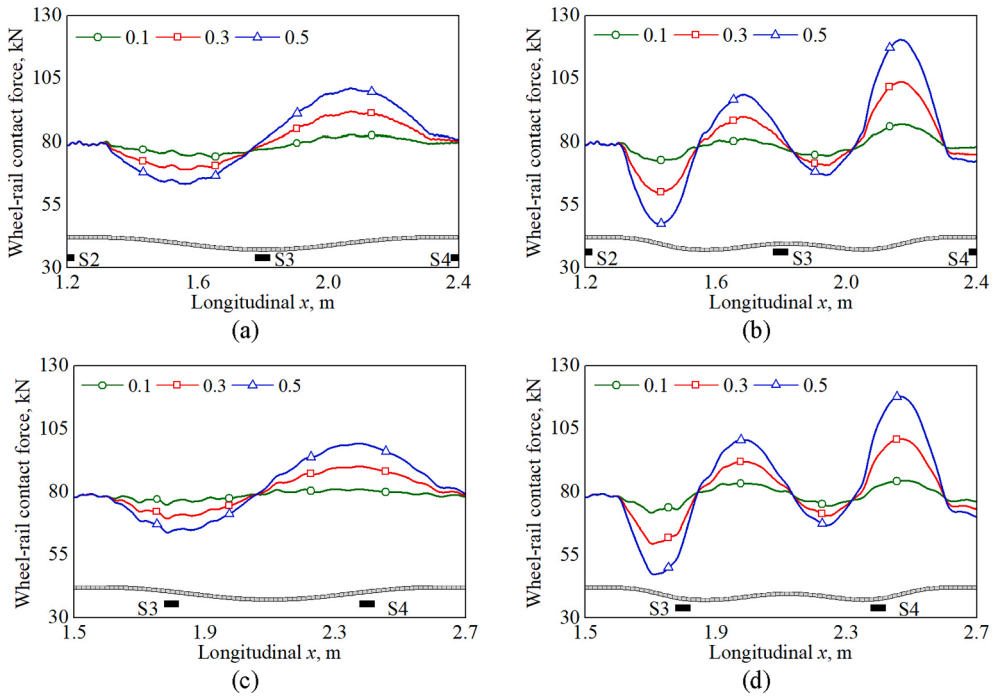

Fig. 6. Wheel-rail normal contact force affected by rail surface irregularities. (a) Unimodal irregularity above sleeper S3. (b) Bimodal irregularity above sleeper S3. (c) Unimodal irregularity in the middle span of sleepers S3 and S4. (d) Bimodal irregularity in the middle span of sleepers S3 and S4.

irregularity is set to 0.25 m, while the parameter a_2 equals $a_1/3$. In the simulation, the train speed is set to 250 km/h, which is the typical operating speed of ballasted HSR in China.

3.1. Wheel-rail normal contact force

Fig. 6 shows the distributions of the wheel-rail normal contact force during the passage of the wheel over rail surface irregularities. Variations of the waveform, depth, and position of the rail surface irregularity are considered. When the rail surface irregularity takes place above sleeper S3 (see Fig. 6(a)-6(b)), the amplitude of the wheel-rail normal contact force increases with the wave depth of the rail irregularity. In the unimodal rail irregularity scenario, the amplitude is 82.6 kN with a wave depth of 0.1 mm and increases by 22.4% to 101.1 kN when the wave depth reaches 0.5 mm. In the bimodal rail irregularity scenario, the influence of the wave depth becomes more significant. For example, when the wave depth increases from 0.1 mm to 0.5 mm, the amplitude of the wheel-rail normal contact force increases from 86.8 kN to 120.2 kN, with a growth of 38.5%.

When the rail surface irregularity moves to the middle span of sleepers S3 and S4 (see Fig. 6(c)-6(d)), the amplitude of the wheel-rail normal contact force also increases with the wave depth of the rail irregularities. When the wave depth equals 0.5 mm, the normal contact force reaches maxima of 99.2 kN and 117.7 kN in the unimodal and bimodal irregularity scenarios, respectively. Comparing Fig. 6(c)-6(d) to Fig. 6(a)-6(b), the amplitude of the wheel-rail impact force is dominated by the geometric characteristics of the rail irregularity, whereas it is less affected by the relative position between the rail irregularity and sleepers.

3.2. Sleeper-ballast normal contact force

Fig. 7 shows the distribution of the sleeper-ballast normal contact force at the rail surface irregularity. In Fig. 7(a), where the unimodal irregularity is above sleeper S3, the sleeper-ballast normal contact force reaches the maximum of 72.6 kN and takes place at sleeper S4. With the growth of wave depth from 0.1 mm to 0.5 mm, the force at sleepers S3 and S4 increases by 38.6% and 36.7%, respectively. In Fig. 7(b), where a bimodal irregularity is above sleeper S3, the maximum of 70.9 kN occurs at sleeper S3 instead of S4. The force at sleepers S3 and S4 increases by 31.7% and 21.3% as the wave depth increases from 0.1 mm to 0.5 mm. The variation in the wave depth of a rail surface irregularity does not greatly affect the sleeper-ballast normal contact force at sleepers S2 and S5.

When the position of rail irregularity moves to the middle span of sleepers S3 and S4, the maximum of the sleeper-ballast normal contact force occurs at sleeper S4 in both the unimodal and bimodal irregularity scenarios (see Fig. 7(c)-7(d)), whereas the maximum shifts to sleeper S3 in Fig. 7(b)). Meanwhile, the presence of the unimodal irregularity in the middle span of sleepers S3 and S4 rarely affects the sleeper-ballast normal contact force at sleeper S3. The relative position between the rail irregularity and sleepers has a

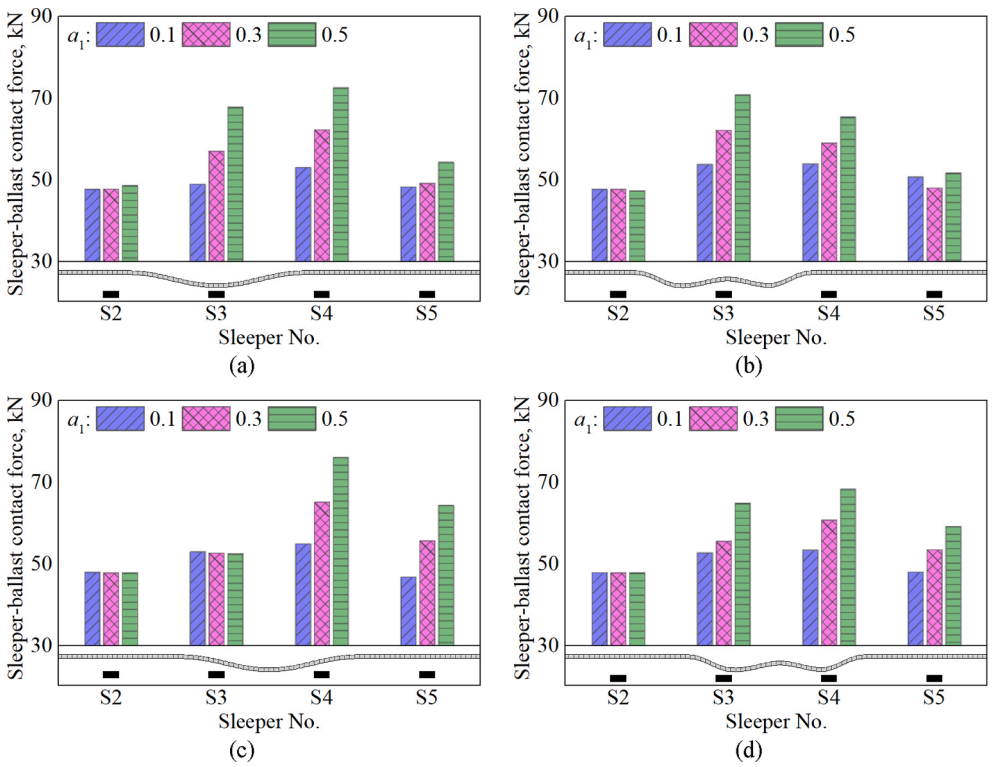

Fig. 7. Sleeper-ballast contact force affected by rail surface irregularities. (a) Unimodal irregularity above sleeper S3. (b) Bimodal irregularity above sleeper S3. (c) Unimodal irregularity in the middle span of sleepers S3-S4. (d) Bimodal irregularity in the middle span of sleepers S3-S4.

significant impact on the distribution of sleeper-ballast normal contact force at sleepers S3 to S5, which differs from the distributions of wheel-rail normal contact force shown in Fig. 6. The magnitude of the sleeper-ballast normal contact force changes significantly between sleepers located at symmetrical positions (e.g., sleepers S3 and S4 in Fig. 7(c)–7(d)), which should be attributed to the differences in the distributions of the wheel-rail normal contact force (see Fig. 6).

3.3. Uneven settlement of the trackbed

Fig. 8 shows the distribution of the trackbed settlement as the total traffic load Q varies from 0.01 to 10 million gross tonnages (MGTs). It is assumed that the axle load remains at a constant value of 16 t, and total traffic loads Q can be transferred to the number of load cycles N via $N = Q/16$. In the figure, the scenario of rail irregularity occurring in the middle span of sleepers S3 and S4 is selected for demonstration purposes, and the depth of the irregularity increases from 0.1 mm to 0.5 mm. The amplitude of the trackbed settlement rises with the growth of both the depth of the rail irregularity and the total traffic loads. Taking sleeper S3 in the scenario of the bimodal irregularity as an example, the trackbed settlement in the case of $Q = 0.01$ MGT and$a_1 = 0.1$ mm is 0.29 mm, which increases by 278% to 1.10 mm in the case of $Q = 0.01$ MGT and$a_1 = 0.5$ mm and further raises by 576% to 1.96 mm in the case of $Q = 10$ MGT and$a_1 = 0.5$ mm. Among all the selected cases, the settlement of the trackbed reaches its maximum at sleeper S4. For example, the trackbed settlement at sleeper S4 reaches 2.04 mm at $Q = 1$ MGT and$a_1 = 0.5$ mm in the scenario of bimodal irregularity, 22.2% and 88.6% larger than the corresponding values at sleepers S3 (1.67 mm) and S5 (1.08 mm), respectively. In addition, it can be observed that the unimodal rail irregularity corresponds to a more significant settlement of the trackbed in comparison to that of the bimodal rail irregularity. Taking sleeper S4 in the case of $Q = 1$ MGT and$a_1 = 0.5$ mm as an example, the trackbed settlement reaches 6.56 mm at the unimodal rail irregularity, which raises by 19% compared to the value at the bimodal rail irregularity (i.e., 5.51 mm).

Fig. 9 shows the uneven settlement of the trackbed when the total traffic load Q reaches 1 MGT. Since the variation in the depth of the rail irregularity has little influence on the sleeper-ballast force at sleeper S2 (see Fig. 7), the settlement of the trackbed at sleeper S2 is specified as a reference to evaluate the uneven settlement behavior. Unimodal irregularity is more likely to aggravate the uneven settlement of the trackbed, regardless of where rail irregularity takes place. In the scenario of rail irregularity with$a_1 = 0.5$ mm occurring above sleeper S3, the uneven settlement of the trackbed reaches a maximum of 2.45 mm at the unimodal irregularity (Fig. 9 (a)), which is 3% higher than the corresponding value (2.37 mm in Fig. 9(b)) at the bimodal irregularity. When the rail irregularity shifts to the middle span of sleepers S3-S4, the uneven settlement increases to 2.93 mm at the unimodal irregularity (Fig. 9(c)), increasing by 44% compared to the value (2.04 mm in Fig. 9(d)) at the bimodal irregularity.

3.4. Status of the sleeper hanging

The uneven settlement of the trackbed serves as an input for the FE simulation of static equilibrium. By comparing the amplitude of

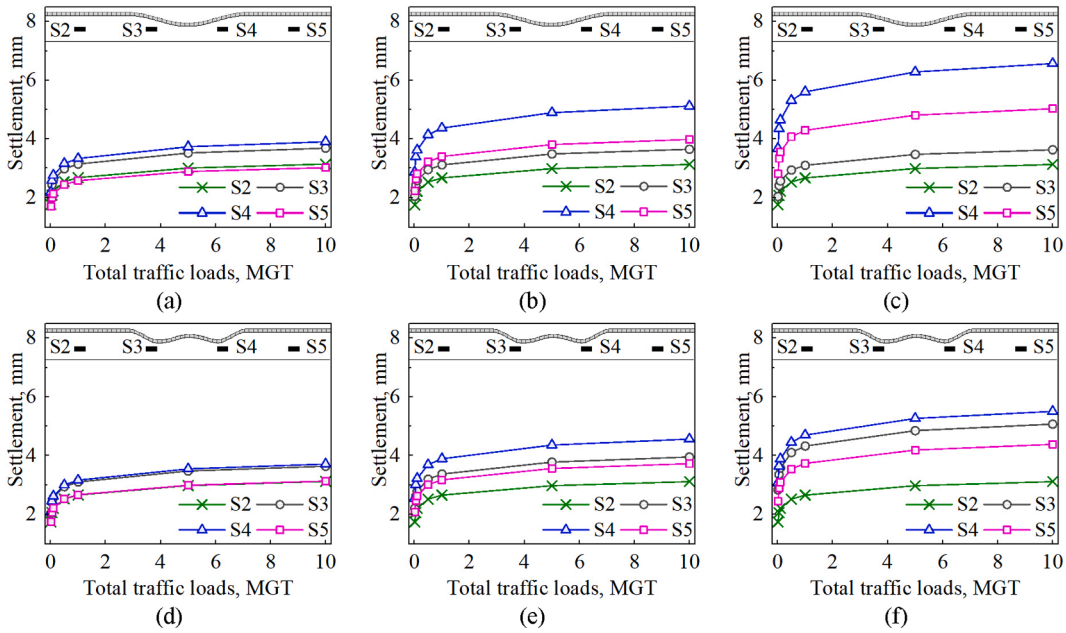

Fig. 8. Settlement of the trackbed induced by the rail irregularity occurring in between sleepers S3 and S4. (a) Unimodal irregularity with a wave depth of 0.1 mm, (b) unimodal irregularity with a wave depth of 0.3 mm, (c) unimodal irregularity with a wave depth of 0.5 mm, (d) bimodal irregularity with a wave depth of 0.1 mm, (e) bimodal irregularity with a wave depth of 0.3 mm, and (f) bimodal irregularity with a wave depth of 0.5 mm.

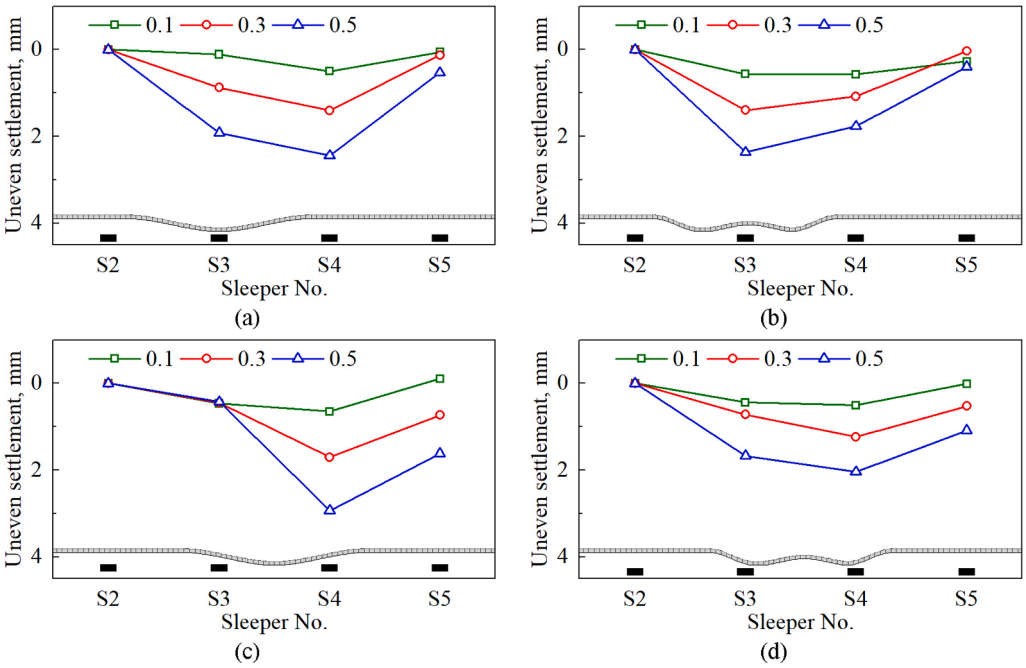

Fig. 9. Uneven settlement of the trackbed induced by rail irregularities. (a) Unimodal irregularity above sleeper S3. (b) Bimodal irregularity above sleeper S3. (c) Unimodal irregularity in the middle span of sleepers S3-S4. (d) Bimodal irregularity in the middle span of sleepers S3-S4.

uneven settlement at sleeper *i* with the initial displacement of the sleeper under gravity, the hanging status of sleeper *i* can be extracted. Table 1 shows the hanging status of sleepers S3 to S5 when the total traffic reaches 1 MGT. In the table, the scenario of bimodal rail irregularity occurring in the middle span of sleepers S3 and S4 is considered for demonstration purposes. Since sleepers S3 ~ S5 are under hanging conditions, the rail deflection above sleeper S4 is larger than that of the neighbors; thus, the initial displacement of sleeper S4 differs from those of sleepers S3 and S5. Sleeper hanging defects take place at almost all the selected sleepers under the specified traffic loads, except for sleeper S5 when the depth of the rail irregularity equals 0.1 mm.

In summary, the geometric characteristics of the rail surface irregularities, such as waveform and depth, significantly influence the distributions of wheel-rail contact force and sleeper-ballast contact force. In particular, the bimodal irregularity induces a more significant wheel-rail impact, while the unimodal irregularity is more likely to aggravate the uneven settlement of the trackbed. References [18,30] pointed out that the wheel-rail impact at the rail surface irregularity contains both high-frequency and mid-/low-frequency components. Since the bimodal irregularity has a shorter wavelength than the unimodal irregularity, its effect on the high-frequency impact becomes more significant. However, the dynamic behavior of the sleepers and the ballast is more closely related to the mid-/low-frequency vibrations. Consequently, the unimodal irregularity contributes more to the rail substructure defects. Meanwhile, the relative position between the rail irregularity and sleepers also largely influences the uneven settlement of the trackbed but has little effect on the wheel-rail contact force.

4. Wheel-rail rolling contact behavior and related rail degradation

The wheel-rail rolling contact behavior during the passage of a wheel over the rail irregularity is simulated, and the contact parameters are extracted to analyze the rail degradation in terms of plastic deformation and RCF [31]. The analysis in this section

Table 1
Hanging status of sleepers S3 to S5 when traffic loads reach 1 MGT.

Sleeper No.	Initial displacement of sleeper $Y^i_{b,s}$/mm	Depth of rail irregularity a_1/mm	Uneven settlement Δu^i_N/mm	Hanging status
S3	0.32	0.1	0.44	Yes
		0.3	0.72	Yes
		0.5	1.67	Yes
S4	0.36	0.1	0.50	Yes
		0.3	1.24	Yes
		0.5	2.04	Yes
S5	0.32	0.1	0.01	No
		0.3	0.52	Yes
		0.5	1.08	Yes

considers that the bimodal rail irregularity has a depth of 0.5 mm and occurs in the middle span of sleepers S3 and S4. The sleeper hanging status when the traffic loads reach 1 MGT is considered.

4.1. Wheel-rail transient contact behavior

Fig. 10 compares the distributions of the wheel-rail normal contact force between normal and sleeper hanging scenarios. For normal sleepers, two peaks of the wheel-rail contact force can be observed at 1.99 m and 2.45 m along the longitudinal direction (P_1=100.5 kN andP_2 = 117.7 kN, respectively). The presence of sleeper hanging raises the peak values by 19.4% and 11.6% (P_1=120.0 kN andP_2 = 131.4 kN), respectively, whereas the positions of the peaks are almost unaffected. It is observed that the distributions of the wheel-rail normal contact force above S2 differ between the two cases, which should be mainly attributed to the change in the initial displacement of the rail. In general, the increase in the wheel-rail contact force and the greater wheel-rail impact energy should speed up rail degradation, which is examined when analyzing the distributions of the plastic deformation and RCF.

In Fig. 11, the contact patches at instants $t_1 \widetilde{t_6}$ (see Fig. 10) are analyzed to gain insight into the wheel-rail contact characteristics. In the scenario with normal sleepers, the size of the contact patch fluctuates slightly at approximately 153 mm^2 at t_1, followed by a drop to 118 mm^2 at t_2. The patch size reaches two peaks of 179 mm^2 and 192 mm^2 at t_3 and t_5 and then shrinks to 153 mm^2 at t_6. When sleepers S3 ~ S5 are hanging, the variation in the patch size becomes more significant. For example, the peaks at t_3 and t_5 are 195 mm^2 and 204 mm^2, raised by 8.9% and 6.3%, respectively. compared to the normal sleeper condition. At the selected instants, the size of the contact patch increases at t_3 and t_5 but decreases at t_2 and t_4, which shows similar trends with the distribution of the wheel-rail contact force. Regarding the portion of the adhesion region in the contact patch, the values under normal sleeper conditions are 69.3% and 71.9% at t_3 and t_5, respectively, and change slightly to 69.2% and 72.5% under hanging sleeper conditions. The results indicate that the presence of sleeper hanging has little effect on the distribution of the adhesion-slip state.

Fig. 12 shows the distribution of pressure and surface shear traction along the longitudinal direction. The shear traction peaks at all the selected instants occur in the rear half of the contact patches. With normal sleepers, the amplitude of the pressure is 989.1 MPa at t_1 and decreases by 10.9% to 881.3 MPa at t_2, followed by two peaks of 1043.3 MPa and 1048.7 MPa at t_3 and t_5, respectively. Under hanging sleeper conditions, the amplitudes at t_3 and t_5 rise by 4.0% and 6.3%, respectively, compared to those of normal sleepers. However, the fluctuation of the surface shear traction is not as significant as the pressure, of which the amplitude varies in the range of 235.2 ~ 269.2 MPa with normal sleepers and the range of 239.8 ~ 285.5 MPa under hanging sleeper conditions.

4.2. Rail degradation

The von Mises (v-M) yield criterion was employed to analyze the deformation of the rail material. Fig. 13 shows the distributions of v-M stress and equivalent v-M strain at instants t_3 and t_5. Under the normal sleeper scenario, there is no plastic deformation at t_3, as the peak value of v-M stress (520.7 MPa) does not exceed the yield strength of 525 MPa. At t_5, the wheel-rail impact force P_2 is greater than the force P_1 at t_3 (see Fig. 10), which promotes the growth of the v-M stress to 534.3 MPa. When sleepers S3 ~ S5 are hanging, the two peaks of the v-M stress (i.e., 527.9 MPa at t_3 and 547.7 MPa at t_5) increases by 1.4% and 2.5%, respectively, in comparison to the normal sleeper scenario, indicating that sleeper hanging could increase the impact energy and exacerbate the plastic deformation of the rail materials.

Regarding the distribution of the equivalent v-M strain, the peaks at t_3 and t_5 are 2.81‰ and 2.95‰ under normal sleeper conditions and increase to 2.87‰ and 3.07‰ when the sleepers are hanging, with growths of 2.1% and 4.1%, respectively. In addition, Fig. 12 shows that the presence of sleeper hanging affects the equivalent v-M strain more than it affects the v-M stress, as the strain grows faster when the v-M stress exceeds the yield strength under the assumption of the bilinear constitutive model of the rail material.

In the literature, the energy dissipation method [32] and the shakedown method [33,34] are commonly used to analyze the presence of RCF. The energy dissipation method accounts for the competitive relation between wear and surface-initiated RCF. However, the method relies on extensive testing and calibration and is currently limited to a few rail steel types. The shakedown method, however, is not restricted to certain wheel/rail steel types. In this study, a surface fatigue index FI_{surf} based on the shakedown

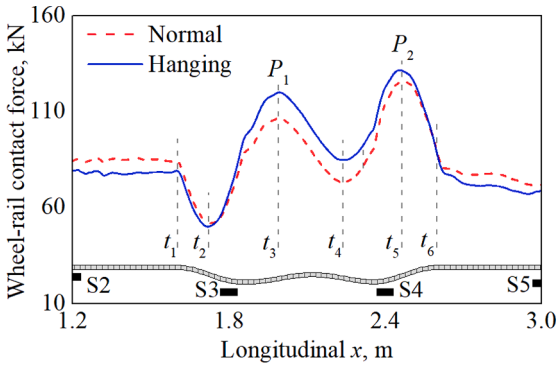

Fig. 10. Effect of sleeper hanging on the wheel-rail contact force.

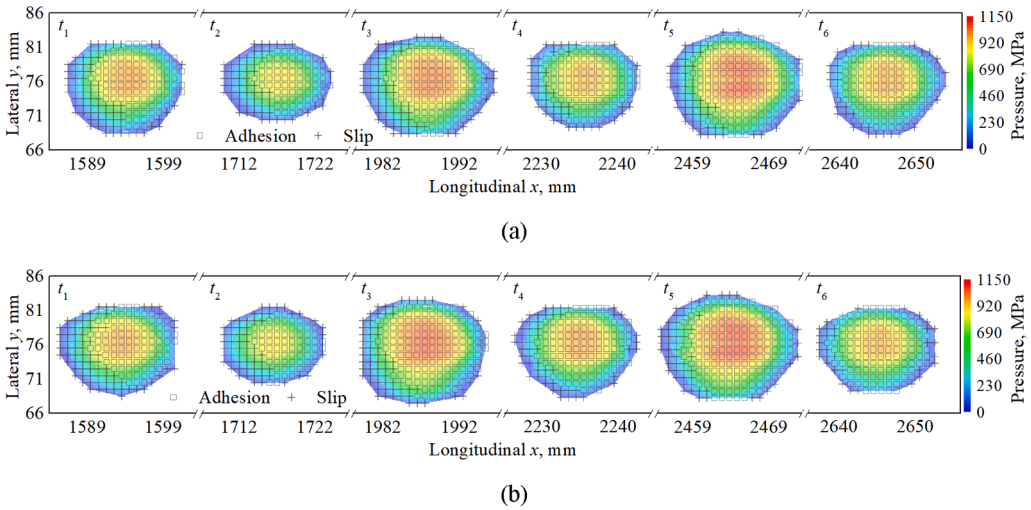

Fig. 11. Effect of sleeper hanging on the contact patch. (a) Normal sleeper condition, (b) Sleeper hanging condition.

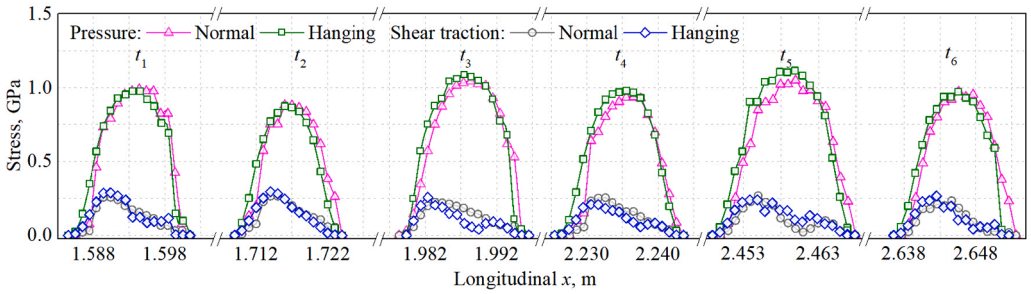

Fig. 12. Effect of sleeper hanging on the contact stresses.

method is employed to analyze the influence of sleeper hanging on the occurrence of RCF in the rail material, expressed as:

$$FI_{\text{surf}} = \left|\frac{F_T}{F_N}\right| - \frac{k}{p_0} \tag{6}$$

where k is the yield strength in shear and p_0 is the maximum pressure in the contact patch. Surface-initiated RCF occurs if $FI_{\text{surf}} > 0$.

Fig. 14 shows the distribution of FI_{surf} along the longitudinal direction. In the figure, the fluctuation of FI_{surf} shows trends similar to those of the wheel-rail contact force, in which two peaks can be observed at approximately t_3 and t_5. The presence of sleeper hanging increases FI_{surf} at these peaks, yet the values are always below zero throughout the region with the rail surface irregularity. The results indicate that the RCF has a small likelihood of occurring on rail surfaces under the specified assumption, regardless of the hanging status of sleepers S3 ~ S5.

4.3. Rail displacement

Generally, the presence of sleeper hanging exacerbates rail displacement during the passage of vehicles, which would adversely affect the safety and stability of train operation. Thus, it is important to analyze the relation between sleeper hanging and rail displacement under wheel loads. Fig. 15 shows the rail vertical displacement when the wheel is rolling over the rail irregularities. In the figure, the maximal displacement in both the normal and sleeper hanging sleeper scenarios occurs approximately at sleeper S4. Under the normal sleeper condition, the maximum ΔY_n is 0.59 mm, increasing by 18.0% compared to the depth of the rail irregularity (i.e., 0.50 mm). When sleepers S3 ~ S5 are hanging, the maximal displacement ΔY_h reaches 2.92 mm, which is 15.0% larger than the sum of the uneven trackbed settlement (2.04 mm) and the depth of the rail irregularity (0.50 mm).

Fig. 16 shows the distributions of the wheel-rail contact force and rail vertical displacement as the depth of the rail irregularities ranges from 0.1 mm to 0.5 mm. For comparison purposes, the sleeper hanging status when the traffic loads reach 1 MGT is attached. The maximal rail displacement is dominated by the depth of the rail surface irregularity under normal sleeper conditions. Once the sleepers are hanging, the rail displacement increases rapidly, where the amplitude of uneven trackbed settlement becomes dominant. Taking the bimodal rail irregularity as an example, the rail displacements under normal sleeper conditions are 0.14 mm, 0.37 mm, and

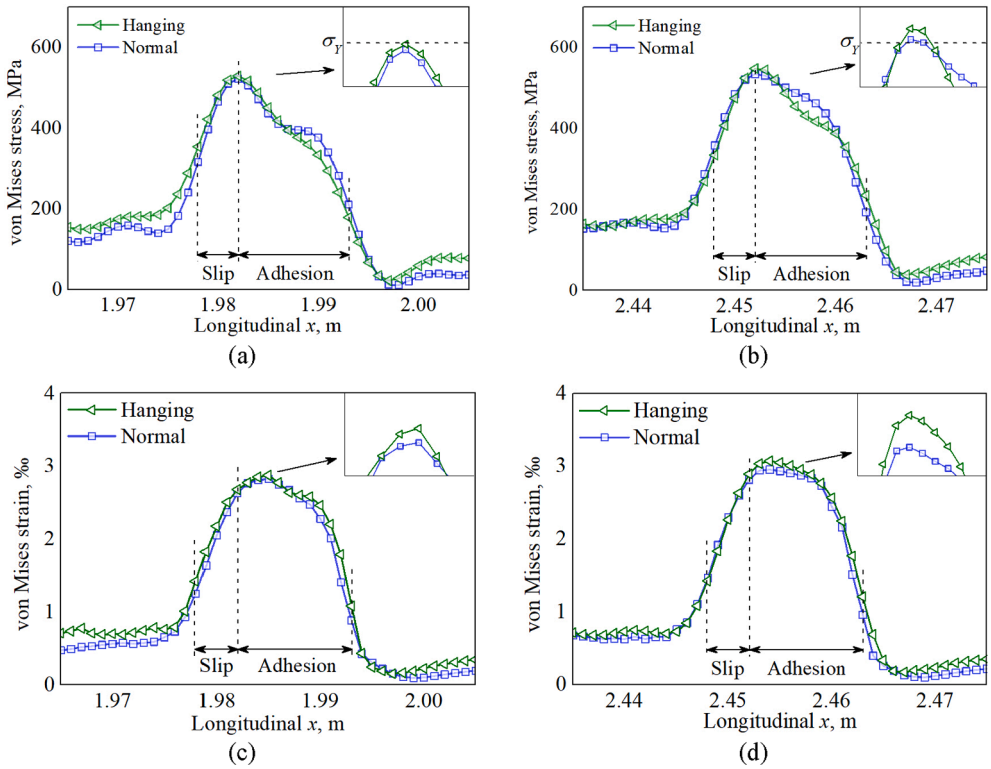

Fig. 13. Effect of sleeper hanging on the distributions of v-M stress and equivalent strain. (a) v-M stress at t_3, (b) v-M stress at t_5, (c) equivalent v-M strain at t_3, (d) equivalent v-M stress at t_5.

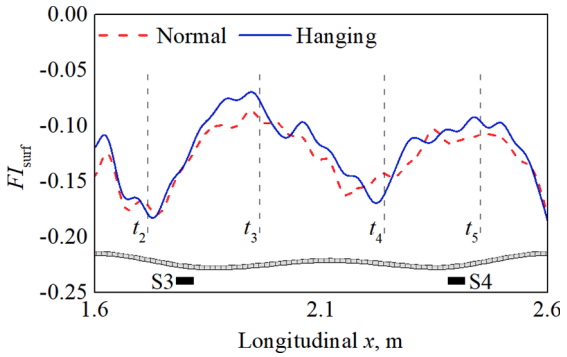

Fig. 14. Effect of sleeper hanging on the surface-initiated RCF.

0.59 mm with rail irregularity depths of 0.1 mm, 0.3 mm, and 0.5 mm, respectively. When the sleepers are hanging, the rail displacements increase by 807.1%, 448.6%, and 394.9% to 1.27 mm, 2.03 mm, and 2.92 mm, respectively. Sleeper hanging also aggravates the maximal wheel-rail contact force, yet the growth rate is much less significant than that of the rail displacement. For example, with the unimodal rail irregularity depths of 0.1 mm, 0.3 mm, and 0.5 mm, the maxima of the wheel-rail contact force in the sleeper hanging scenario increase by 4.2%, 8.1%, and 9.0%, respectively, compared with those in the normal scenario.

5. Conclusions

This study analyzes the sleeper hanging defects induced by a rail surface irregularity and their consequence on the wheel-rail rolling contact behavior. For this purpose, a wheel-rail transient rolling contact model capable of accounting for the nonlinear displacement-force properties of sleeper hanging sleeper is developed. The uneven settlement of the trackbed under specified traffic loads is extracted to identify the sleeper hanging status. After that, the wheel-rail contact parameters such as contact force and stresses, contact patch, and von Mises stress are analyzed, and the rail degradation in terms of plastic deformation and RCF is evaluated. The

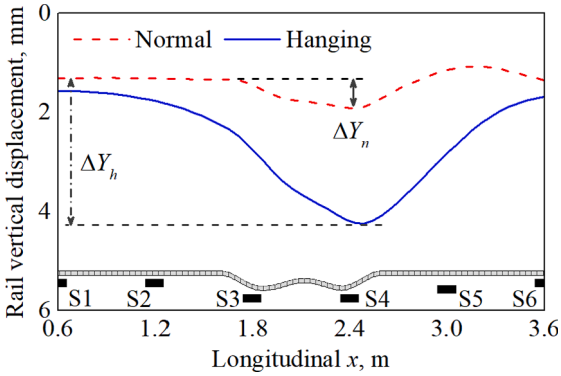

Fig. 15. Effect of sleeper hanging on the rail displacement.

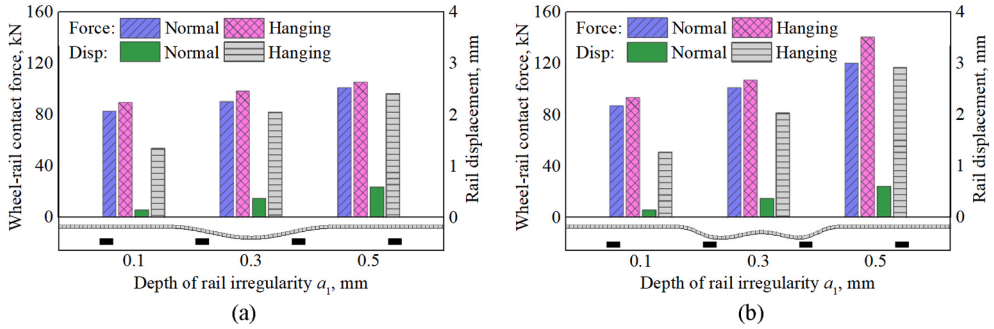

Fig. 16. Effect of sleeper hanging on the dynamic wheel-rail contact, (a) maximal rail displacement, and (b) maximal wheel-rail contact force.

main conclusions are drawn as follows:

(1) The presence of the initial deformation on the rail surface aggravates the uneven settlement of the trackbed, and the amplitude of uneven settlement increases with the depth of the rail irregularity and traffic loads.
(2) The unimodal rail irregularity is more likely to exacerbate the uneven settlement of the trackbed than the bimodal irregularity, whereas the latter would induce a more significant wheel-rail impact.
(3) The relative position of the rail surface irregularity and sleepers has a significant influence on the uneven settlement of the trackbed but has little effect on the magnitude of the wheel-rail normal contact force.
(4) The presence of sleeper hanging increases the amplitudes of the wheel-rail contact force, contact patch size, and contact stresses, whereas it has little effect on the portion of the adhesion-slip region in the contact patch.
(5) The rail material would suffer from more severe plastic deformation when the sleepers are hanging, while RCF has little likelihood of occurring under the assumption of the specified traffic loads.
(6) The sleeper hanging defects drastically increase the rail vertical displacement during the passage of vehicles. When the total traffic load reaches 1 MGT, the rail displacement coexcited by the sleeper hanging and rail surface irregularities would be three times larger than that in the normal sleeper condition.

In future work, more generalized geometric characteristics of rail surface irregularities will be analyzed by accounting for the randomness and variations of wavelength, waveform, and other variables that were assumed fixed in this study. Meanwhile, the analysis of the trackbed settlement in this study relies on the sleeper-ballast interaction at the first loading cycle, whereas the interaction, in reality, would change based on the sleeper hanging status. Thus, an iterative computation method should be considered to simulate the dynamic evolution process of sleeper hanging defects.

Declaration of Competing Interest

The authors declare that they have no known competing financial interests or personal relationships that could have appeared to influence the work reported in this paper.

Acknowledgments

This study is supported by the Scientific Research Plan of China Railway No. K2019G010 as well as the Science and Technology Research Plan of China Academy of Railway Sciences No. 2020YJ063.

References

[1] S. Grassie, S. Cox, The dynamic response of railway track with unsupported sleepers, Proc. Inst. Mech. Eng. Part D: J. Automobile Eng. 199 (1985) 123–136.
[2] S. Kaewunruen, A.M. Remennikov, Effect of improper ballast packing/tamping on dynamic behaviors of on-track railway concrete sleeper, Int. J. Struct. Stab. Dyn. 7 (2007) 167–177.
[3] Kaewunruen S, Remennikov AM. Investigation of free vibrations of voided concrete sleepers in railway track system. Proceedings of the Institution of Mechanical Engineers, Part F: J. Rail Rapid Transit. 2007;221:495–507.
[4] Lundqvist A, Dahlberg T. Load impact on railway track due to unsupported sleepers. Proceedings of the Institution of Mechanical Engineers, Part F: J. Rail Rapid Transit. 2005;219:67–77.
[5] J.Y. Zhu, D.J. Thompson, C.J.C. Jones, On the effect of unsupported sleepers on the dynamic behaviour of a railway track, Veh. Syst. Dyn. 49 (2011) 1389–1408.
[6] A.M. Recuero, J.L. Escalona, A.A. Shabana, Finite-element analysis of unsupported sleepers using three-dimensional wheel–rail contact formulation, Proc. Inst. Mech. Eng. Part K: J. Multi-body Dyn. 225 (2011) 153–165.
[7] Rezaei E, Dahlberg T. Dynamic behaviour of an in situ partially supported concrete railway sleeper. Proceedings of the Institution of Mechanical Engineers, Part F: J. Rail Rapid Transit. 2011;225:501–508.
[8] J. Shi, A.H. Chan, M.P. Burrow, Influence of unsupported sleepers on the dynamic response of a heavy haul railway embankment, Proceedings of the Institution of Mechanical Engineers Part F Journal of Rail & Rapid Transit. 227 (2013) 657–667.
[9] M. Sadri, T. Lu, M. Steenbergen, Railway track degradation: The contribution of a spatially variant support stiffness - Local variation, J. Sound Vib. 455 (2019) 203–220.
[10] M. Sadri, T. Lu, M. Steenbergen, Railway track degradation: The contribution of a spatially variant support stiffness - Global variation, J. Sound Vib. 464 (2020), 114992.
[11] J.J. Zhu, A.K.W. Ahmed, S. Rakheja, A. Khajepour, Development of a vehicle–track model assembly and numerical method for simulation of wheel–rail dynamic interaction due to unsupported sleepers, Veh. Syst. Dyn. 48 (2010) 1535–1552.
[12] Dahlberg T. Some railroad settlement models—A critical review. Proceedings of the Institution of Mechanical Engineers, Part F: J. Rail Rapid Transit. 2001;215: 289–300.
[13] Varandas JN, Hölscher P, Silva MA. Settlement of ballasted track under traffic loading: application to transition zones. Proceedings of the Institution of Mechanical Engineers, Part F: J. Rail Rapid Transit. 2013;228:242–259.
[14] J. Piotrowski, W. Kik, A simplified model of wheel/rail contact mechanics for non-Hertzian problems and its application in rail vehicle dynamic simulations, Veh. Syst. Dyn. 46 (2008) 27–48.
[15] J.J. Kalker, A fast algorithm for the simplified theory of rolling contact, Veh. Syst. Dyn. 11 (1982) 1–13.
[16] J.J. Kalker, Three-dimensional elastic bodies in rolling contact, Kluwer Academic Publishers, Dordrecht, Netherlands, 1990.
[17] Z. Li, X. Zhao, R. Dollevoet, M. Molodova, Differential wear and plastic deformation as causes of squat at track local stiffness change combined with other track short defects, Veh. Syst. Dyn. 46 (2008) 237–246.
[18] X. Zhao, Z. Li, R. Dollevoet, The vertical and the longitudinal dynamic responses of the vehicle–track system to squat-type short wavelength irregularity, Veh. Syst. Dyn. 51 (2013) 1918–1937.
[19] M. Molodova, Z. Li, R. Dollevoet, Axle box acceleration: Measurement and simulation for detection of short track defects, Wear 271 (2011) 349–356.
[20] Z. Yang, A. Boogaard, Z. Wei, J. Liu, R. Dollevoet, Z. Li, Numerical study of wheel-rail impact contact solutions at an insulated rail joint, Int. J. Mech. Sci. 138–139 (2018) 310–322.
[21] B. An, P. Wang, J. Xiao, J. Xu, R. Chen, Dynamic response of wheel-rail interaction at rail weld in high-speed railway, Shock Vib. 2017 (2017) 5634726.
[22] Z. Wei, A. Núñez, A. Boogaard, R. Dollevoet, Z. Li, Method for evaluating the performance of railway crossing rails after long-term service, Tribol. Int. 123 (2018) 337–348.
[23] X. Zhao, Z. Wen, M. Zhu, X. Jin, A study on high-speed rolling contact between a wheel and a contaminated rail, Veh. Syst. Dyn. 52 (2014) 1270–1287.
[24] Z. Yang, X. Deng, Z. Li, Numerical modeling of dynamic frictional rolling contact with an explicit finite element method, Tribol. Int. 129 (2019) 214–231.
[25] X. Zhao, Z. Wen, H. Wang, X. Jin, 3D transient finite element model for high-speed wheel-rail rolling contact and its application, Journal of Mechanical Engineering. 49 (2014) 1–7.
[26] Y. Sato, Japanese Studies on Deterioration of Ballasted Track, Veh. Syst. Dyn. 24 (1995) 197–208.
[27] L. Mauer, An Interactive Track-Train Dynamic Model for Calculation of Track Error Growth, Veh. Syst. Dyn. 24 (1995) 209–221.
[28] H. Zhou, Z. Bao, S. Zhang, Dynamical evolution process of voided sleeper, J. Tongji Univ. (Natural Science) 47 (2019) 521–527.
[29] J.N. Varandas, P. Hölscher, M.A.G. Silva, Dynamic behaviour of railway tracks on transitions zones, Comput. Struct. 89 (2011) 1468–1479.
[30] H.H. Jenkins, J.E. Stephenson, G.A. Clayton, G.W. Morland, D. Lyon, The effect of track and vehicle parameters on wheel/rail vertical dynamic forces, Rail. Eng. J. 3 (1974).
[31] Z. Wei, A. Núñez, X. Liu, R. Dollevoet, Z. Li, Multi-criteria evaluation of wheel/rail degradation at railway crossings, Tribol. Int. 144 (2020), 106107.
[32] M. Hiensch, M. Steenbergen, Rolling Contact Fatigue on premium rail grades: damage function development from field data, Wear 394 (2018) 187–194.
[33] A. Ekberg, E. Kabo, Fatigue of railway wheels and rails under rolling contact and thermal loading—an overview, Wear 258 (2005) 1288–1300.
[34] A. Ekberg, E. Kabo, H. Andersson, An engineering model for prediction of rolling contact fatigue of railway wheels, Fatigue Fract. Eng. Mater. Struct. 25 (2002) 899–909.